Detailed Characterization of SWIR-sensitive Colloidal Quantum Dot Image Sensors

Joo Hyoung Kim[1], Vladimir Pejovic[1,2], Epimitheas Georgitzikis[1], Yunlong Li[1], Pawel E. Malinowski[1], Itai Liebermann[1], David Cheyns[1], Paul Heremans[1,2], and Jiwon Lee[1]

[1]imec, Kapeldreef 75, 3001 Leuven, Belgium
[2]KU Leuven, 3001 Leuven, Belgium
Email: Jiwon.Lee@imec.be, Tel.: +32 477 963078

***Abstract*— Due to the poor responsivity of Si imagers to photons with energy lower than 1.12 eV, thin-film-based image sensors are getting more attention as an alternative imaging platform. Among the promising absorbers, lead sulfide (PbS) Colloidal Quantum Dot (CQD) photodetectors are highlighted with their absorption wavelength peak tunability up to 2.6 µm, and compatibility with CMOS process. However, despite marvelous innovations in QD imagers, few results have been discussed regarding their imager characteristics in detail. In this work, elaborate analyses on our shot-noise-limited and Short-Wavelength-Infrared (SWIR) sensitive PbS CQD imagers are presented, giving special emphasis on their state-of-the-art SWIR QD imager EQE up to 40% at 1450 nm wavelength. Operation speed is estimated by image lag characterization and suppressed blooming behavior by the restricted lateral movement of photo-generated charge carrier within the transport layer (TL) of the photodiode (PD) stack. Finally, we have demonstrated how activation energy for CQD can be statistically analyzed by dark current spectroscopy.**

***Index Terms*—Thin-film imager, PbS Colloidal Quantum dot photodiode, SWIR-sensitive, Dark current spectroscopy, shot-noise-limited**

I. Introduction

As the spectral information with photon energy less then 1.12 eV (Si bandgap) is getting more importance in both industrial and scientific fields [1], thin-film-based image sensors have been studied as one of the candidates for the next-generation imaging platform for this spectral range [2]. From all the promising absorbers of light longer than 1 µm wavelengths, CQD is highlighted with its capability of monolithic wafer-level integration, which offers potentially high manufacturing throughput compatible to the standard CMOS Si 200/300 mm processes, cost-effectiveness, and smaller pixel pitch down to 1.82 µm for SWIR imagers since CQD imager fabrication is not restricted by the flip-chip process used for III-V / II-VI / hybrid bulk crystalline photodetectors such as InGaAs [3]. Among all CQD members, PbS was adopted to our devices, a material which is well investigated and more air-resistant compared to other QD materials, featured with its absorption wavelength peak tunability up to 2.6 µm, encompassing SWIR spectral region of light [4]. However, despite of tremendous innovations in the thin-film-based imager development, few detailed imager-level characterization results have been discussed.

Therefore, in this work, many interesting SWIR-sensitive PbS CQD imager features are presented. Shot-noise-limited Photon Transfer Curve (PTC) behaviors are found in the strong light illumination condition, with special emphasis on the state-of-the-art SWIR QD imager EQE at 1450 nm peak absorption wavelength [6]. Operation speed is estimated by image lag measurements, without losing speed performance of CQD Photodiode (PD) by the integration of imager ROIC. Suppressed blooming phenomena can be seen by the compressed lateral movements of the photo-generated charge carrier within the transport layer for the PD stack. Finally, pixel-by-pixel dark current spectroscopy reveals the presence of multiple inter-bandgap generation centers of CQD PD layer.

II. Experiments and Results

Our PbS CQD imagers were developed by optimizing their ROIC designs and QD stack fabrication processes, especially monolithic integration onto the Si ROICs with record-breaking pixel pitch down to 1.82 µm for imagers dedicated to SWIR spectral range (Fig.1) [5]. Typical PTC data for the developed prototype SWIR image sensor, which contains 768×512 pixels with 5µm pitch, shows shot-noise-limited behavior in the relatively intense light illumination regime (Fig. 2), where its overall imager characteristics are given in Table 1. EQE spectra were measured and compared from the PbS CQD imager to its passive PD-only device, sharing similar spectral shape and their measured values, most featured with the SWIR QD imager state-of-the-art ~40% of EQE at 1450 nm peak absorption wavelength (Fig. 3). This means that the spectral photoresponsivity has been well preserved with the addition of imager ROIC structure.

A picture taken by our image sensor integrated with SWIR long pass filter is also presented, displaying dark sky despite visibly sunny weather, due to little scattering cross section of photons in this spectral range by small air molecules via Rayleigh scattering ($\sim\lambda^{-4}$), while clouds look more apparent for more electromagnetic radiation is scattered in this wavelength region by larger water droplets mediated by Mie scattering

(poor dependence on the incident light wavelength, Fig 4(a)). This shows stark contrast to the image taken with the integration of the visible light short pass filter (Fig. 4(b)). SWIR sensitivity of our imager can be found once again with more controlled set of objects, by distinguishing two plastic bars, one rendered to have more SWIR light scattering surface (Fig. 4 (c) bright, bottom), and the other with more SWIR absorbing one (dark, top), which are ill-distinguished under the illumination of visible light due to much less scattering of light on the surfaces of bars in this spectral range (Fig. 4(d)).

A. Image lag

To quantify speed performance of this thin-film-based imager, image lag is estimated by measuring the signal of the remaining photo-generated charge carriers from the fully saturated bygone frame by changing reset time from 10ns to 10ms. A non-observable image lag was found when we drain accumulated charge carriers from the lapsed frame for longer than 208.5 μs. This is comparable to the fall time from 100% to 0.4% (read-out noise level) of the signal for a passive test PD-only device, while 100% to 10% decay time is 6.5 μs, significantly faster compared to the values shown in literatures (Fig. 5, Table 2) [6]. Even with this order of reset time duration, with digital CDS operation by keeping the reset transistor on during non-integration time, frame rate up to 50 fps could be achieved for our imager with 768x512 pixel array.

B. Blooming

Blooming for our thin-film devices is characterized along with various composition of PD stacks, by comparing sensitivities from two different measurement configuration. First, sensitivity at no intended blooming configuration mode was estimated (top, Fig 6(a)), and it is compared to the case where neighboring pixels are saturated that the photo-generated charge carriers were set to overflow to the pixel which is selected to read out signal (bottom, Fig 6(a)). In this way, intended electrical crosstalk can be quantified. To get deeper understanding with these measurements, blooming from different stack compositions were compared, displaying correlation to the conductivities of the transport layers for each stack configuration, which might imply that the major cause for blooming would be related to the lateral movement of photo-generated charge carriers within the transport layer of the PD stack in the out of the vertical electric field biased between the top and the bottom electrodes. Since the voltage configuration is the same between the pixel being read out and the saturated neighboring pixels regardless of the change in the transport layers, we expect more overflowing current from fully charged pixel to the relatively empty pixel under interest for transport layers with higher conductivity (Fig. 6(b)) [7].

For the PD stack used in our most updated version, estimated blooming value was the smallest compared to other candidate stack configurations, probably due to the restricted lateral movements of photo-generated charge carriers within the transport layer in use. Even for the case of the chemically identical inorganic transport layers, doped ones have shown more blooming behavior than the undoped ones, which might be described by the increased overflowing current from neighboring pixels to the read-out pixel, by the reduced resistivity of the transport layer, whereas the potential difference between these pixels is not changed regardless of dopant concentration of the TL.

C. Dark Current Spectroscopy

Dark current spectroscopy is performed for further understanding of distribution of dark charge carrier generation centers of our PbS CQD PD (Fig. 7). The estimated activation energy from whole chip is ~0.41 eV, close to the mid-bandgap energy of our PbS CQD material (Fig 8, peak absorption wavelength 1450 nm: bandgap of ~0.86 eV). This result suggests that the generation centers of our SWIR-sensitive QD are mainly located around the mid-bandgap energy level, and this mechanism is more trap-assisted rather than bulk generation of the light absorbing structure [8]. Utilizing data acquisition availability from individual pixels, activation energy for each pixel is calculated and statistically analyzed, showing multiple activation energy peaks ranging from 0.23 eV to 0.43 eV (statistically prominent peak, Fig. 9). This suggests a promising capability for statistical studies regarding inter-bandgap states of thin-film light absorbers, which is a great advantage for imagers with large number of pixels.

III. Conclusion

In this paper, we have demonstrated SWIR-sensitive PbS CQD imagers and compared the photoresponsivity of imagers to their PD-only counterparts. Preservation of both temporal and spectral photoresponse have been confirmed, with the achievement of state-of-the-art EQE for imagers made from QD photon absorbing layers. We statistically configured how generation centers of the PD stack are energetically distributed, which is a strength of imagers with sub-million-pixel number. We can apply this methodology to enhance performance of thin film image sensors to target specifications in terms of defect engineering beyond the current state-of-the-art SWIR image sensors, with an outlook for a more facile fabrication and possibility to cost-sensitive applications.

References

[1] C. Livache *et al., Front. Chem.* 2018, 6, 575.
[2] P. E. Malinowski *et al., Proc. SPIE 11765, Optical Architectures for Displays and Sensing in Augmented, Virtual, and Mixed Reality (AR, VR, MR) II*, 2021, 117650V; doi: 10.1117/12.2584144
[3] J. Lee *et al., 2020 IEEE International Electron Devices Meeting (IEDM)*, 2020, 16.5.1-16.5.4.
[4] C. Dong *et al., ACS Appl. Mater. Interfaces* 2019, 11, 47, 44451–44457
[5] V. Pejović *et al., IEEE Electron Device Letters 2021*, doi: 10.1109/LED.2021.3093081
[6] X. Yin *et al., J. Mater. Chem. C*, 2021,9, 417-438
[7] B. Sun *et al., Nano Lett.* 2020, 20, 3694−3702
[8] Z. Jin *et al., Sci Rep*, 2016, 6, 37106
[9] S. Cheylan *et al., J. Appl. Phys.* 2008, 103, 096110
[10] K. BOČKUTĖ *et al., Mat. Sci.* 2013, 19, 3, 245-249
[11] I. Saurdi *et al., AIP Conf. Proc.* 1963, 2018, 020054

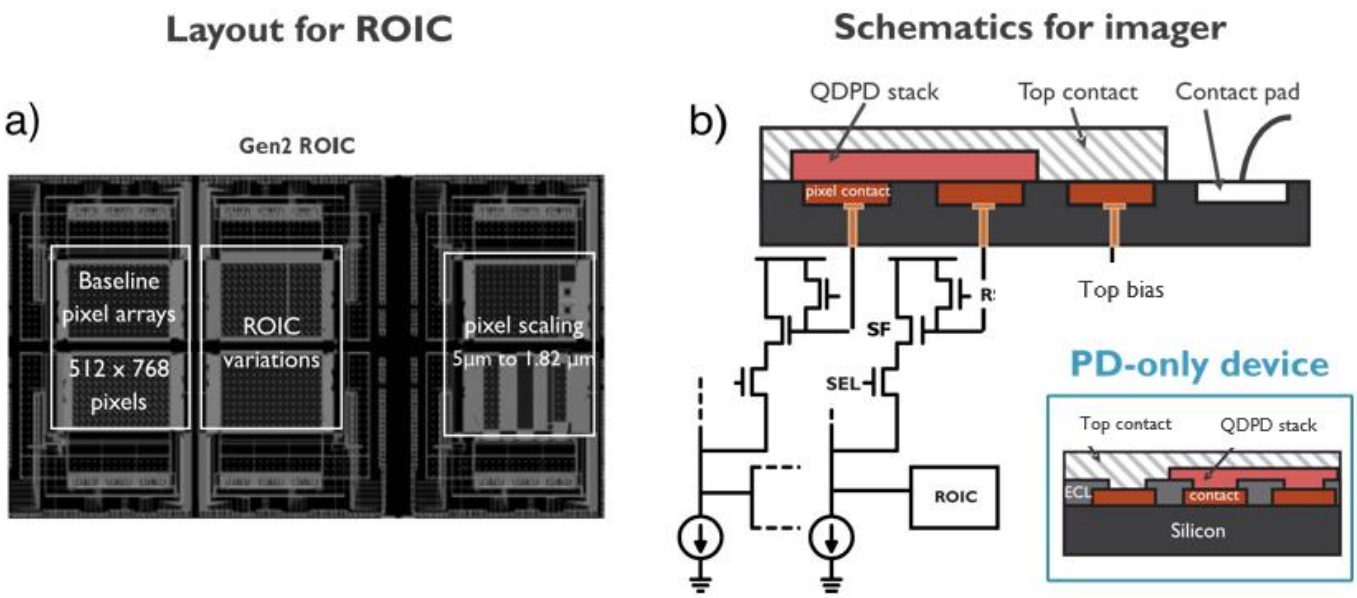

Figure 1. (a) Layout for Si ROIC of our PbS QDPD imager. (b) QDPD stack integration on Si ROIC, and the structure schematic of its passive test PD-only device without ROIC (inset).

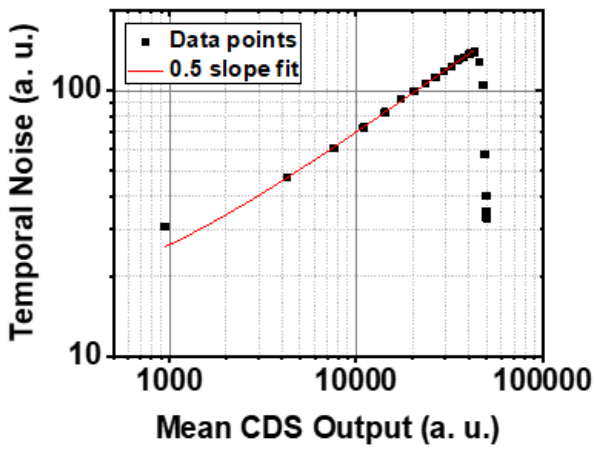

Figure 2. Typical PTC curve for our PbS QDPD Imager displaying shot-noise limited behaviour under the relatively intense light illumination condition.

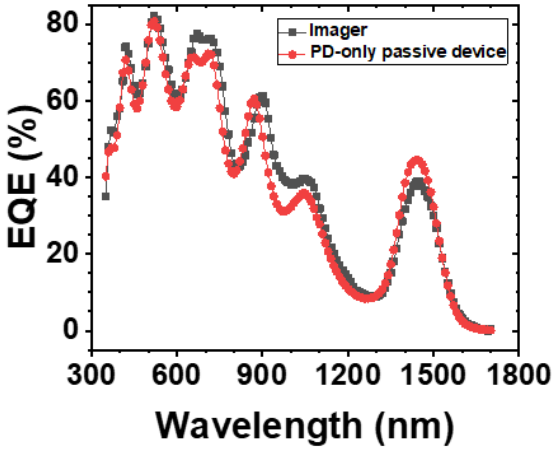

Figure 3. EQE measured with a PD-only passive device (red), with an imager (black), with no significant change in the spectral shape.

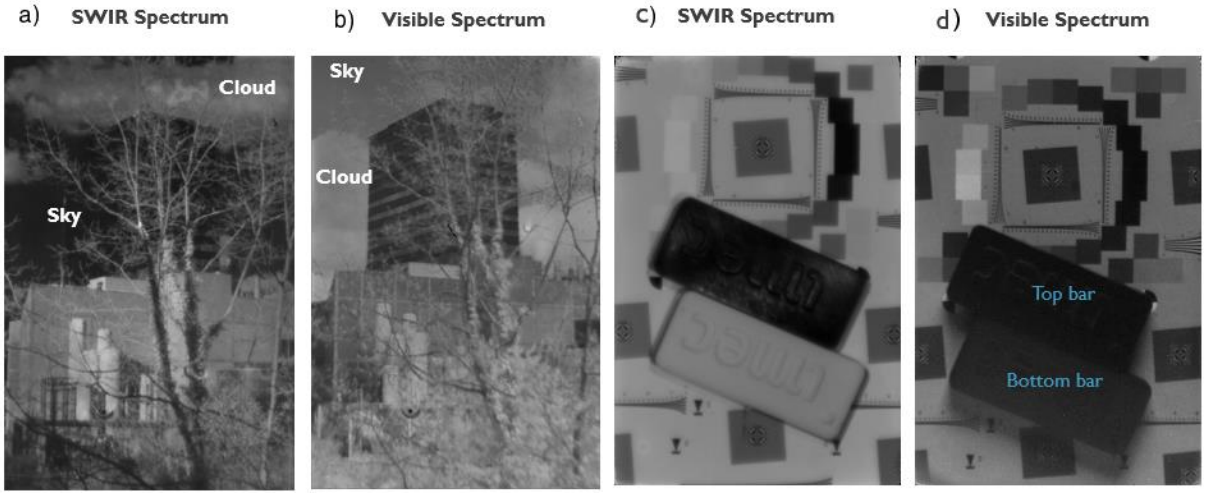

Figure 4. Image of imec campus taken with our QDPD imager on a visibly sunny day in the SWIR spectral range (a), and visible one (b). Set of images capturing objects intended to optically more distinguishing, under the illumination of both visible and SWIR light with good image quality where bottom plastic bar shown brighter by the surface rendered to scatter more SWIR light, compared to the more SWIR absorbing top plastic bar (dark) with the integration of SWIR long-pass filter (c), while less apparent distinction observed between two bars integrated with visible short-pass filter (d). Images taken after multiple dark current spectroscopy measurements with varying temperature from -20°C to 80°C within thermal chamber for longer than 36 hours.

Table 1. PbS QD Image Sensor Characteristics

PARAMETER	Pixel Pitch (μm)	Array Size (px)	CG (μV/e$^-$)	DR (dB)	PD Swing (V)
VALUE	5	768×512	9.526	72	0.7
PARAMETER	FWC (e$^-$)	Dark Current (A/cm^2)	PRNU (%)	RN (e$^-$)	
VALUE	101,000	2.0×10^{-6}	2.8	25	

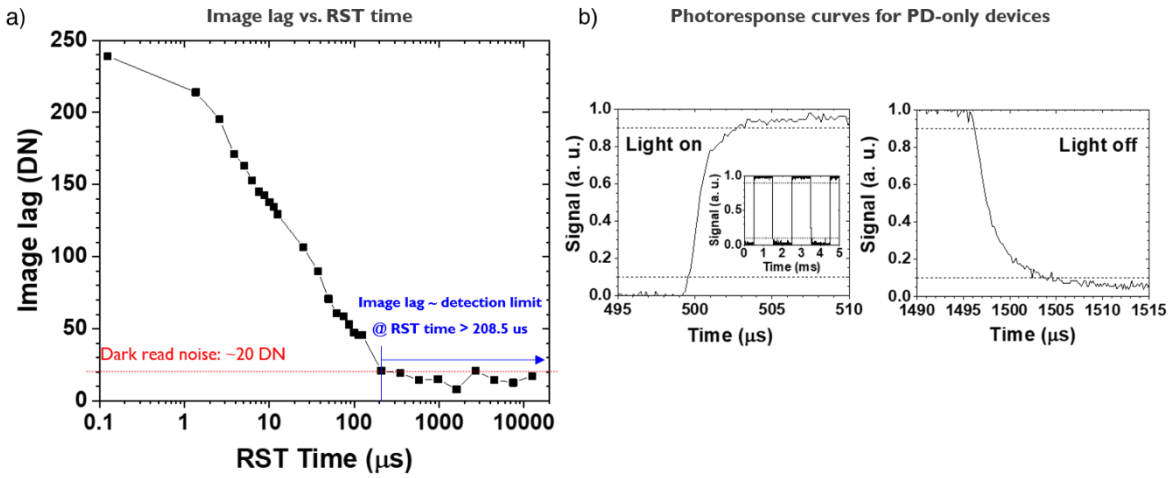

Figure 5. (a) Image lag change according to the reset time length. No observable image ghost found with the application of the reset time longer than 208.5 μs, (b) which is comparable to 100% to 0.4% fall time of the PD-only device (right). Typical rising behavior of PD (left), and its 2.5 cycles of rise & decay profiles (inset, left) given as well.

Table 2. Comparison of speed performance between PbS QDPD & imager

Level	Rise time (PD)	Fall time (PD)	Reset time (Imager)
10%↔90%	3.4 μs	8.9 μs	-
0%→99.96% (100%→0.04%)	145.8 μs	396.7 μs	> 208.5 μs

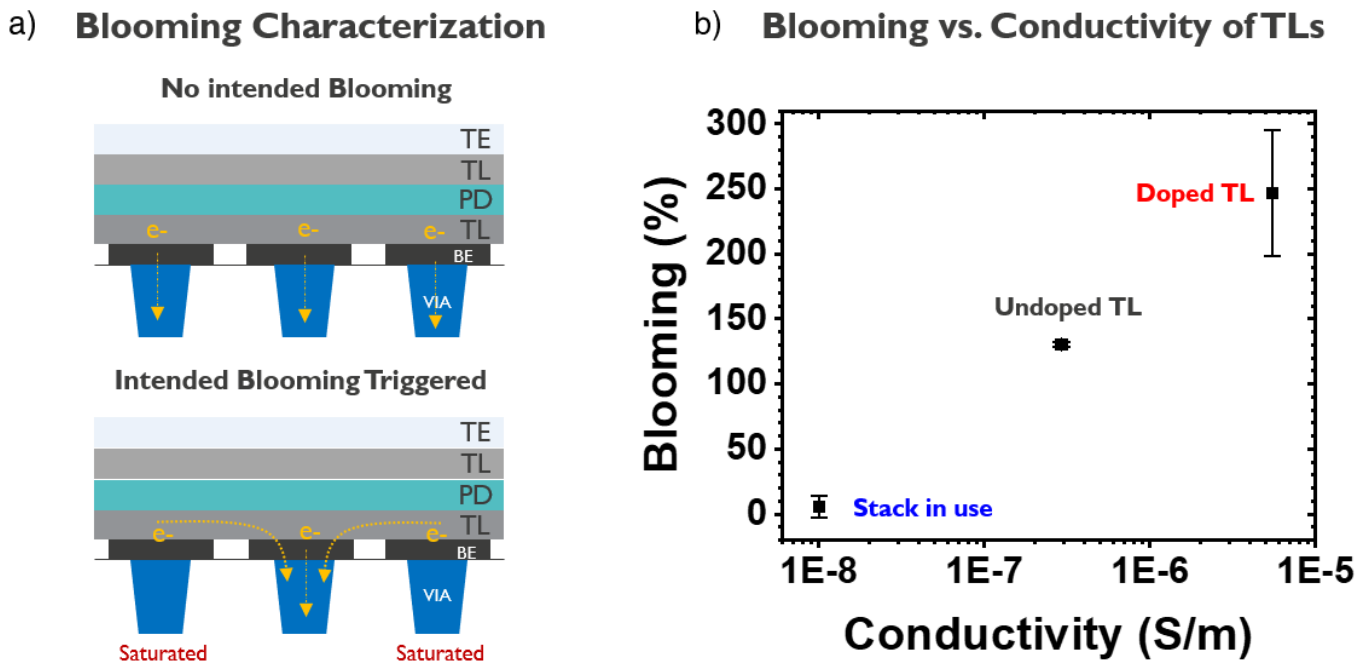

Figure 6. (a) Measurement scheme for characterization of Blooming with our thin-film-based imager. (b) Blooming vs. conductivity of different transport layers. Conductivity values adopted from literatures [9-11].

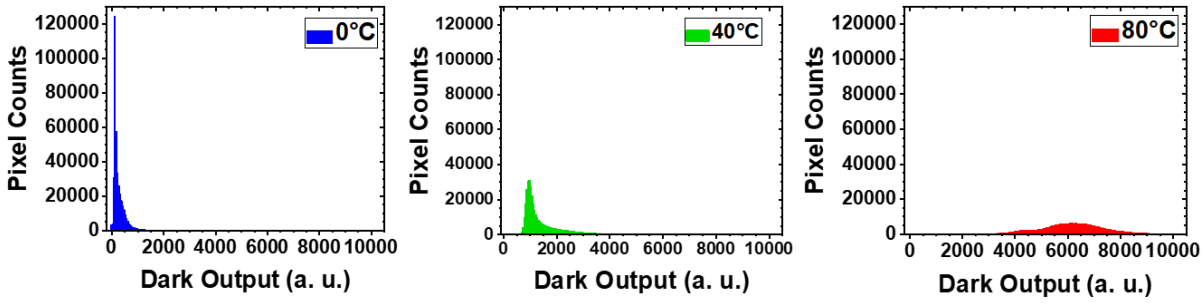

Figure 7. Dark output propagation along with increasing temperature.

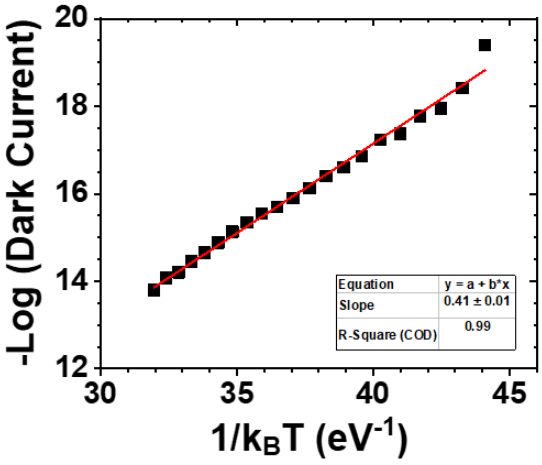

Figure 8. Arrhenius plot from PbS CQD imager pixel data. ~0.41 eV of activation energy is fitted from this plot.

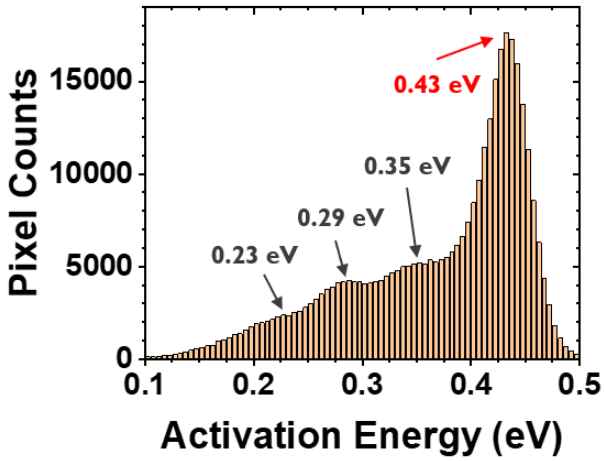

Figure 9. Activation energy histogram computed from individual pixels, showing multiple peaks ranging from 0.23 eV to 0.43 eV.